Excited oscillons: Cascading levels and higher multipoles

Yi-Jie Wang,[1,*] Qi-Xin Xie,[1,†] and Shuang-Yong Zhou[1,2,‡]

[1]*Interdisciplinary Center for Theoretical Study, University of Science and Technology of China, Hefei, Anhui 230026, China*

[2]*Peng Huanwu Center for Fundamental Theory, Hefei, Anhui 230026, China*

(Received 30 March 2023; accepted 13 June 2023; published 10 July 2023)

We investigate two types of excited oscillons. We first focus on spherical symmetry and find that there are a tower of spherical oscillons with higher energies. Despite having multiple approximate "nodes" in their energy density profiles, these oscillons are long-lived. We find that during the lifetime of an excited oscillon it will cascade down all of the lower energy levels before its disintegration, with each level-dropping period accompanied by a short burst of energy. We also point out the existence of excited oscillons with higher approximate multipoles, which generally have shorter lifespans than the spherical ones. Apart from performing nonlinear simulations with absorbing boundary conditions, we also apply a perturbative method to analyze some features of these excited oscillons.

DOI: 10.1103/PhysRevD.108.025006

I. INTRODUCTION

While topological defects such as sine-Gordon kinks are easy to find in $1+1$ dimensions, Derrick's theorem dictates that (smooth) localized *static* solutions are bound to be unstable for a canonical scalar field with a potential in more than $1+1$ dimensions [1]. Stable localized solutions do exist in higher dimensions, in the form of Q-balls [2–4], if the scalar is endowed with an internal symmetry and one settles to *stationary* solutions that are time periodic. Nevertheless, even in the case of a real scalar field, there are some localized objects that are like Q-balls but quasiperiodic and live for a long time, nowadays known as oscillons [5,6].

Oscillons commonly exist in models that admit potentials with attractive self-interactions, which translates to some relatively mild conditions on the flatness of the potential, similar to the conditions for the Q-balls to exist [3,4]. The properties of oscillons have been extensively studied over the years; see, e.g., Refs. [7–42]. Indeed, the current cosmological observations indicate that the inflaton potential may be very flat [43], and oscillons can be copiously generated in the reheating period after inflation or in other similar processes in the early Universe [44–57]. The presence of oscillons can affect the big bang thermal history and lead to an oscillon-dominated epoch. The production of oscillons in the early Universe is often accompanied by stochastic gravitational waves that characterize the energy scales and other features of the underlying model [58–70]. The oscillon preheating scenario has also been investigated in full numerical relativity [38,56,69], and it was found that primordial black holes can sometimes form from them in the case of strong gravity effects [38,56]. Furthermore, oscillons in $2+1$ dimensions have been observed in laboratories [71–73].

In this paper, we search for and investigate oscillons that are excited in two "orthogonal" ways. First, we focus on excited oscillons in spherically symmetry. We find that there are excited oscillons with increasing levels of energy, whose oscillation frequency decreases with the level of energy. As the evolution of an oscillon is a process where its (dominant) oscillation frequency adiabatically increases until it reaches the upper limit and dissipates, these different energy plateaus naturally appear in sequence in the evolution history of a highly excited oscillon, forming a rather intriguing cascade (see Fig. 1). These higher-energy oscillons are solutions with increasingly more (approximate) nodes, and the lifespans of these plateaus decrease with their energies. We also provide a semianalytic computation of the lifespans of the plateaus by simply approximating the oscillon with a factorizable background plus the leading perturbative radiation field, which matches the nonlinear simulations rather well.

Excited spherical Q-balls with multinode structures have been studied in Refs. [74–78]. The spherical oscillons we study in this paper are actually different

*yjwang@mail.ustc.edu.cn
†xqx2018@mail.ustc.edu.cn
‡zhoushy@ustc.edu.cn

in spirit, apart from the difference between complex and real scalars. The equivalent spherical oscillons similar to those excited Q-balls can also be constructed, as we briefly discuss in this paper, but those strongly multinode spherical oscillons are much shorter lived than our weakly multinode ones. This is most easily seen in the perturbative construction where our spherical oscillons can be approximated by an unexcited background plus a leading multinode perturbation.

Second, we construct nonspherical oscillons that are excited to have higher multipoles. These oscillons may arise from anisotropic environments or from collisions of oscillons, perhaps similar to the fact that astrophysical black holes generally have spin. At any rate, these are nonlinear localized objects with interesting properties that are worth exploring. Nonspherical Q-balls, the counterparts for the case of a complex scalar field, were recently studied in the form of charge-swapping Q-balls [79–81] or spinning Q-balls and their generalizations in the presence of gauge fields or strong gravitational effects [74,82–92]. Whereas one can construct a Q-ball with a fixed multipole, this is impossible for an oscillon which, nevertheless (as we will show), can have a dominant multipole supported by some weak subdominant ones. Therefore, unlike a Q-ball whose profile is factorizable into a radial part plus a rotation phase, a multipolar oscillon is generally more complex in nature.

To numerically construct a spinning oscillon, one can take a factorized configuration as the input, and we see that it can then relax to the spinning solution. We find that it is imperative to prepare the initial configuration to at least solve the background equation of motion. This suggests that the "attractor basin" for spinning oscillons is relatively small, compared to the spherical case, where one can obtain excited oscillons from quite generic configurations. Also, for higher multipolar oscillons, we only find spinning oscillons but not the swapping ones. This is due to the fact that for the case of oscillons the real scalar field only has one component, while for the case of Q-balls the complex field has two components. Because of this, the latter can be intuitively viewed as two interconnected oscillons, which allows one to arrange attracting, opposite-charge lumps to form charge-swapping Q-balls [79]. These results show that the similarities between oscillons and Q-balls are also shared by their composite/excited structures, with some major caveats as well.

The paper is organized as follows. In Sec. II we introduce the model we focus on in this paper and the perturbative expansion we use for the semianalytical computations later. We describe the numerical codes we use for the fully nonlinear simulations in Appendix A and some technical details about the perturbative expansion in Appendix B. In Sec. III we investigate properties of spherical cascading oscillons including their evolution patterns, lifetimes, insensitivity to initial conditions, and spectra. The efficient spherical code used in this section is validated by the full-blown Cartesian code in Appendix C. We also perform a perturbative analysis to compute the lifespans of the various energy plateaus of the cascading oscillons. In Sec. IV we investigate another type of excited oscillons, which have higher multipoles. The simulations in this section are performed with a Cartesian code with absorbing boundary conditions. We conclude and describe possible phenomenological implications in Sec. V.

II. MODEL AND SETUP

We focus on oscillons from the simplest model with only one real scalar field φ that is invariant under reflection $\varphi \to -\varphi$. As we will see, this simple model already gives rise to rich time evolutions and complex structures that are quasistationary. From the modern, prevailing point of view of effective field theory, such a theory in $d+1$ dimensions is given by the action

$$\tilde{S} = \int \mathrm{d}^{d+1}\tilde{x}\left(-\frac{1}{2}\partial_{\tilde{\mu}}\varphi\partial^{\tilde{\mu}}\varphi - \frac{1}{2}m^2\varphi^2 + \lambda\varphi^4 - g_0\varphi^6 + g_1\varphi^8 + g_2(\partial_{\tilde{\mu}}\varphi\partial^{\tilde{\mu}}\varphi)^2 + \cdots\right), \tag{1}$$

where m is the mass of the scalar and the mass dimensions of the coupling constants are $[\lambda] = 3-d$, $[g_0] = 4-2d$, $[g_1] = 5-3d$, $[g_2] = -d-1$, and so on. (One may add terms like $\partial^4\varphi^2$ and $\partial^2\varphi^4$, but these terms can be removed by field redefinitions.) For simplicity, in this paper we truncate to the order of φ^6 in the Lagrangian. Making use of dimensionless variables

$$x^\mu = m\tilde{x}^\mu, \quad \phi = \frac{(2\lambda)^{1/2}\varphi}{m}, \quad g = \frac{m^2 g_0}{2\lambda^2}, \tag{2}$$

the truncated action can be rewritten as

$$\begin{aligned} S &= \frac{m^{3-d}}{2\lambda}\int \mathrm{d}^{d+1}x\mathcal{L} \\ &\equiv \frac{m^{3-d}}{2\lambda}\int \mathrm{d}^{d+1}x\left(-\frac{1}{2}\partial_\mu\phi\partial^\mu\phi - \frac{1}{2}\phi^2 + \frac{1}{2}\phi^4 - \frac{1}{2}g\phi^6\right). \end{aligned} \tag{3}$$

This leaves us with just one dimensionless free parameter g in the model,[1] and we explore the dependence of the phenomena on this parameter. Results for models with different hierarchies between m and λ can be extracted by appropriate scalings. For the simple case with no hierarchy between m and λ (say, $m^{3-d} = 2\lambda$), one can view the values

[1]In $2+1$ dimensions, the φ^4 term is relevant with λ having mass dimension $[\lambda] = 1$ and the φ^6 term is marginal, so S is apparently renormalizable.

of all of the dimensionful quantities in this paper as in units of the mass of the scalar. The (rescaled) energy density Legendre transformed from $\mathcal{L}$ is given by

$$\mathcal{H} = \frac{1}{2}\dot{\phi}^2 + \frac{1}{2}(\nabla\phi)^2 + \frac{1}{2}\phi^2 - \frac{1}{2}\phi^4 + \frac{1}{2}g\phi^6, \tag{4}$$

where the dot stands for the partial derivative with respect to t, and the equation of motion is given by

$$\ddot{\phi} - \nabla^2\phi + \phi - 2\phi^3 + 3g\phi^5 = 0. \tag{5}$$

As discussed in the Introduction, the action (3) supports quasistable oscillons, which are nonlinear, localized quasisolitons that exist in many field theories having shallow potentials. Unlike a Q-ball solution that exists in a complex scalar theory, a spherically symmetric oscillon for a real scalar does not simply factorize to a spatial profile and a temporal oscillation. Rather, the oscillon solution Fourier decomposes into a spectrum of multiple modes, although, as we will see later, many of its interesting properties can be described by the dominant one, with the higher-frequency modes determining the decay rate of the oscillon. We will also see that there exist a series of excited spherical oscillons, which naturally emerge as different phases that a highly excited oscillon goes through during its entire lifetime. In addition to spherically symmetric oscillons, in Sec. IV we will see that there are also complex oscillons that contain higher multipoles and may be viewed as the real scalar counterparts of charge-swapping Q-balls [79–81] and spinning Q-balls [74,82–92]. We will later construct and simulate these solutions fully nonlinearly.

The simulation schemes we use in this paper are explained in Appendix A. In Sec. III, where we focus on spherically symmetric oscillons and perform multiple parameter scans, we use a spherical grid code, which is more efficient as it is essentially a $1+1$D code whose absorbing boundary conditions are easier to implement. A spherical code, however, neglects the effects of nonspherical perturbations. In Appendix C we compare a typical evolution in the spherical code with that in the Cartesian code, and show that the effects of nonspherical perturbations are negligible for our case. On the other hand, all of the simulations in Sec. IV are run with the Cartesian code, as we will deal with higher multipolar configurations there.

To help construct the complex, excited oscillons and understand their properties semianalytically, we use the following mode expansion that can capture many salient features of these solutions in $2+1$D:

$$\phi(t,r,\theta) = \Phi_{l_0}(r) r^{l_0}\cos(\omega t - l_0\theta) + \sum_{n>1,|l|>l_0} A_n^l(r) r^{|l|}\cos(n\omega t - l\theta), \tag{6}$$

where l_0, l, n are integers (with $n>1$ and $l_0 \geq 0$)[2] and we have factored out r^l such that regularity at $r=0$ requires that

$$\partial_r\Phi_{l_0}(r=0) = 0, \qquad \partial_r A_n^l(r=0) = 0. \tag{7}$$

This expansion for the $l_0 = 0$ case was previously adopted in Ref. [93] for investigating the lowest-energy spherical oscillons. As assumed in the mode expansion (6), which will be verified later, an oscillon solution usually has a dominant oscillation frequency ω, whose amplitude $\Phi_{l_0}(r)$ can be viewed as the *background* amplitude, and the *perturbations* around this factorizable background have frequencies that are mostly multiples of the base frequency. For a higher multipolar oscillon ($l_0 \neq 0$), as will be explained later, the background mode needs to be spinning in one direction, such as $\cos(\omega t - l_0\theta)$. By examining the equations of motion explicitly (see Appendix B), one can also show that when the background is spinning in one direction, the opposite-spinning perturbative modes are decoupled (and unexcited), so in Eq. (6) we can restrict l to be $l > l_0$ in the summation without loss of generality.

For later convenience, we write the nonlinear terms in the equations of motion as $F(\phi) \equiv -2\phi^3 + 3g\phi^5$, and define $C_n^l(r)$ and $B_n^l(r)$ as the coefficient functions in the following expansions:

$$F(\Phi_{l_0} r^{l_0}\cos(\omega t - l_0\theta)) = \sum_{i\geq 0} C_{2i+1}^{(2i+1)l_0}(r)\cos((2i+1)\omega t - (2i+1)l_0\theta), \tag{8}$$

$$F'(\Phi_{l_0} r^{l_0}\cos(\omega t - l_0\theta)) = \sum_{i\geq 0} B_{2i}^{2il_0}(r)\cos(2i\omega t - 2il_0\theta). \tag{9}$$

For example, we have $C_1^{l_0} = -\frac{3}{2} r^{3l_0}(\Phi_{l_0})^3 + \frac{15}{8} g r^{5l_0}(\Phi_{l_0})^5$ and $B_0^0 = -3r^{2l_0}(\Phi_{l_0})^2 + \frac{45}{8} g r^{4l_0}(\Phi_{l_0})^4$. Then, the background equation of motion is given by

$$\partial_r^2\Phi_{l_0} + \frac{2l_0+1}{r}\partial_r\Phi_{l_0} + (\omega^2 - 1)\Phi_{l_0} - \frac{C_1^{l_0}}{r^{l_0}} = 0, \tag{10}$$

and the perturbative equations of motion are given by

$$\partial_r^2 A_n^l + \frac{2l+1}{r}\partial_r A_n^l + (n^2\omega^2 - 1 - B_0^0)A_n^l - \frac{C_n^l}{r^l} - \frac{1}{2r^l}\left(\sum_{j=2}^{\infty} B_j^{jl_0} r^{l+jl_0} A_{n+j}^{l+jl_0} + \sum_{j=2}^{n-2} B_j^{jl_0} r^{l-jl_0} A_{n-j}^{l-jl_0}\right) = 0. \tag{11}$$

[2]Negative l_0 is of course allowed, representing an opposite-spinning background, but we restrict l_0 to be non-negative for simplicity since the theory is parity invariant.

The presence of only a single angular momentum mode in the background field implies that many of the perturbative fields are actually unexcited. From the definitions of C_n^l and B_n^l above [Eqs. (8) and (9)], we see that $C_{2i}^l = 0$ and $B_{2i+1}^l = 0$, so the equations of motion for A_{2i}^l are decoupled from those of A_{2i+1}^l and are unsourced (i.e., without the inhomogeneous term in their equations of motion), leading to $A_{2i}^l = 0$. Additionally, all of the $A_n^{nl_0+k}$ modes with nonzero k are unsourced, and are thus also unexcited. (The equations of motion for $A_n^{nl_0+k}$ with different k are decoupled from each other, and only the $A_n^{nl_0}$ modes are sourced; see Appendix B for more details.)

The background field Φ_{l_0} and perturbative fields A_n^l can be solved with standard ordinary differential equation (ODE) solvers. As Φ_{l_0} falls off to zero very fast asymptotically at large r, going like $e^{-\sqrt{1-\omega^2}r}/r^{(2l_0+1)/2}$, the background equation (10) can be easily solved by a standard shooting method, shooting from near $r = 0$ to a large r. On the other hand, from the perturbative equations of motion (11), we see that the radiation field A_n^l falls off to zero much more slowly and oscillatorily at large r, going like $H_b(r) \propto J_l(\sqrt{n^2\omega^2 - 1}r)/r^l \sim \cos(\sqrt{n^2\omega^2 - 1}r - (2l + 1)\pi/4)/r^{l+1/2}$, where J_l is the Bessel function of the first kind. (It is also possible to have a solution that includes the Bessel function of the second kind, but that only affects the solution by a constant phase in the cosine, which does not affect the radiation rate we are after in this paper.) Therefore, to accurately solve Eq. (11), we use a shooting procedure where we shoot from a small r to a relatively large $r = r_b$ and match the value of $A_n^l(r_b)/\partial_r A_n^l(r_b)$ to the value of $H(r_b)/\partial_r H(r_b)$ at r_b.

III. CASCADING OSCILLONS

In this section we focus on composite structures in spherically symmetric oscillons. We will see that there are excited oscillons whose energy decays cascadingly with time, forming a series of descending steps, and we explore their properties and explain this phenomena with a semi-analytical mode expansion. In this section, since we are interested in spherically symmetric solutions, we make use of a spherical code, which makes it easier to set up the absorbing conditions at the boundaries and is much computationally cheaper. This of course has the danger of neglecting nonspherical modes in the evolutions. In Appendix C we validate our approach with full Cartesian simulations and show that the nonspherical modes are negligible in these simulations.

A. Cascading levels

To construct excited spherically symmetric oscillons, we set up a (2D or 3D) spherical initial configuration:

$$\phi = Ae^{-\frac{(r^2-a)^2}{\sigma^2}}, \qquad \dot{\phi} = 0, \tag{12}$$

where A sets the amplitude of the field, σ is the thickness of the spherical shell, and a determines the radius from the center. This Gaussian-like initial setup is of course for convenience (as excited oscillons can form starting from more generic configurations), and it will initially relax and shed a certain amount of energy, as we see in Fig. 1. When excited oscillons are properly formed, they are more radially complex, as we see in Figs. 2 and 3. Nevertheless, the relaxed configuration still continuously radiates away energy, and thus the absorbing boundary conditions discussed in Appendix A are useful to eliminate the unwanted fluctuations in the simulation grid.

Figure 1 shows a typical evolution of the total energy E [defined in Eq. (13)] of such an oscillon. Numerically, we define the energy of the oscillons by integrating over the energy density for all of the points within a radius of $R = 20$ from the center of the oscillon:

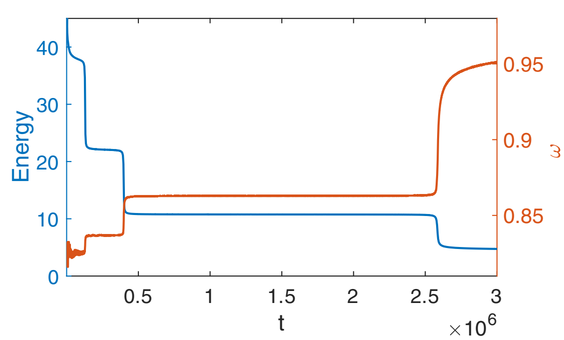

(a) 2+1D

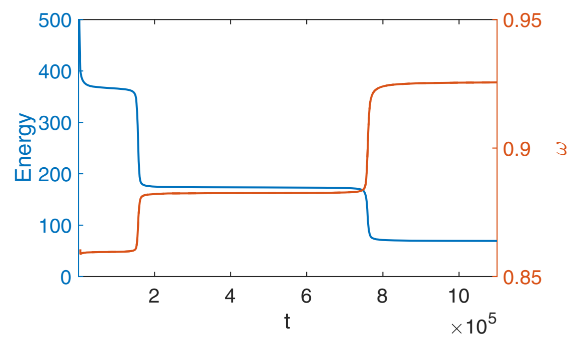

(b) 3+1D

FIG. 1. Cascading levels of the energy E [defined in Eq. (13)] and frequency ω [defined to be the (angular) frequency of a point in the center of the oscillon] of a spherically symmetric oscillon. We can see multiple distinct energy plateau levels as the oscillon evolves, and the frequencies of the levels increase as the energy steps down. The initial configuration is chosen to have $A = 1, a = 81, \sigma = 90$, and the coupling is $g = 0.60$. We label the energy levels from the lowest (the first level) to the highest.

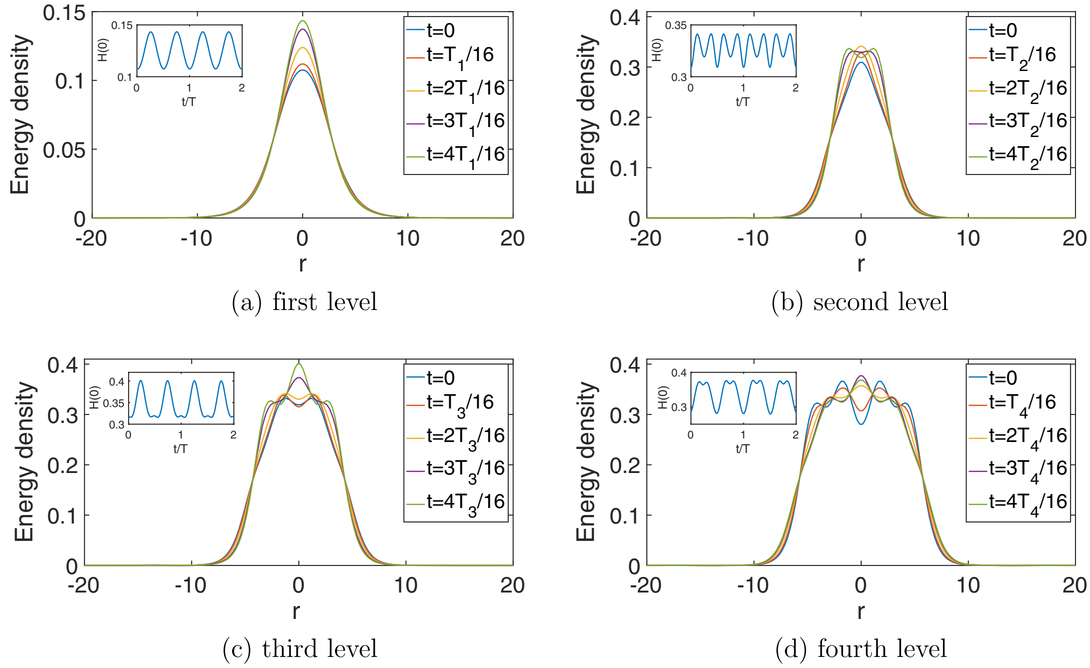

FIG. 2. Evolution of the energy density $\mathcal{H}(t,r)$ of the four plateau levels of the $2+1$D oscillon in Fig. 1(a). T_1, T_2, T_3, T_4 are the oscillation periods of the field ϕ at the center of the oscillon, respectively, with T_1 being that of the first energy level. The oscillation period of the energy density is half of the corresponding period of the field. The insets show the time evolutions of the energy density at $r=0$.

$$E(t)=\int_{r<R}\mathrm{d}^d x\mathcal{H}(t,r). \tag{13}$$

The energy density of a spherical oscillon typically halves at around $r\simeq 2.5$–5. We can see an interesting phenomenon that the energy E of the oscillon cascades with time, producing multiple levels/plateaus before settling down to the most (quasi)stable level. We do not see a sudden decay of the most stable level in the $2+1$D simulations for this particular model, but the oscillon does continuously radiate slowly, which is well known (e.g., Ref. [6]). As we can see in Fig. 1, the excited higher-energy levels live for much shorter times, and (as will be explained shortly in Figs. 2 and 3) they have increasingly more "nodes" in their radial profile.[3] We can also see that during the evolution within an energy level the dominant (angular) frequency of the oscillon ω is stable, where the frequency ω is numerically defined as the frequency of the grid point that initially has the largest field amplitude, i.e., a point in the center of the oscillon. Also, the energy and frequency levels match.

The higher-energy plateaus have more nodes. Take the $2+1$D case, for example; in Fig. 2(a), we see that the radial energy profile has one node at $r\simeq 2.63$, while in Fig. 2(d) we have four nodes at $r\simeq 1.13$, 2.63, 3.62, 5.75. While some nodes such as the outermost node are not moving in the oscillation, conforming to the exact definition of a node, some other nodes do move slightly and are less well defined. Remarkably, the peak densities of the excited plateau levels have roughly similar values, which are noticeably greater than that of the first level. The increase in energy from the second level to the fourth level is mainly due to the oscillon being fatter for the higher levels. Visually, in Fig. 2 we see that the evolution of the energy density of the excited oscillons exhibits the effects of breathing in and out. This is also technically true for the first-level oscillon, due to the presence of a node, but it is less visually obvious (it is more noticeable for the first-level oscillon in the $3+1$D case). Incidentally, for the setup in Fig. 1, the energy levels are $E\simeq 38$, 22, 11, 6, which are mostly twice of the "base" energy level $E\simeq 6$. For a different coupling constant g, the gap between the first level and the second level will change accordingly, but the pattern of the gaps between the higher levels seems to remain. This presumably is due to the fact that the higher-energy levels come from the increase of the number of nodes in the solution, i.e., from the energy density profile becoming fatter, with the factor of 2 coming from the fact that the spatial dimension is 2. In Fig. 3, we see that the $3+1$D case is very similar. In the following, we focus on the $2+1$D case for simplicity.

In our model (3), there is only one theory parameter: the coupling g. (To obtain the behaviors of the solution for

[3]Here, the term "node" is used in a loose sense, and it is not the point where the field profile remains zero at all times. By a node, we mean a point in the energy density profile that visually oscillates less than the surrounding points; see Figs. 2 and 3.

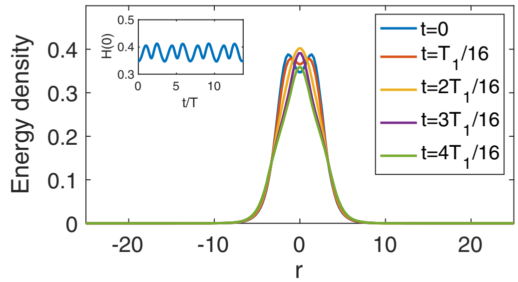

(a) first level

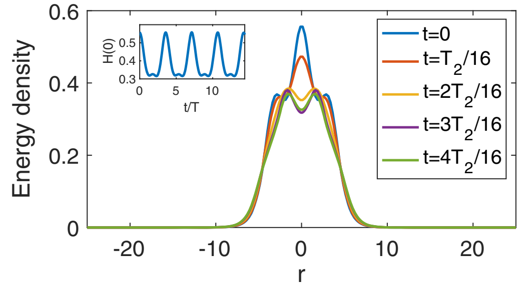

(b) second level

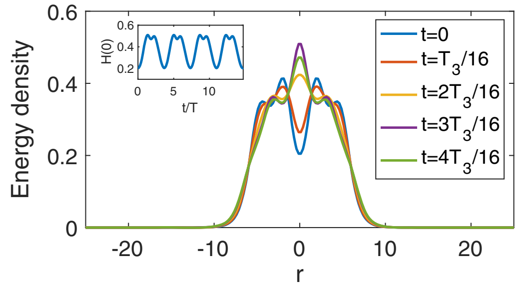

(c) third level

FIG. 3. Evolution of the energy density $\mathcal{H}(t, r)$ of the three plateau levels of the $3+1$D oscillon in Fig. 1(b). T_1, T_2, T_3 are the oscillation periods of the field ϕ at the center of the oscillon, respectively, with T_1 being that of the first energy level. The oscillation period of the energy density is half of the corresponding period of the field. The insets show the time evolutions of the energy density at $r = 0$.

different masses and φ^4 couplings, we can simply scale the units of the solution.) It is instructive to see how the excited oscillons depend on this parameter. In Fig. 4, we plot the dependence of the energy levels on the coupling g. We see that for a larger coupling the excited energy levels exist for much longer times, but the values of the energy levels only vary slightly for different g. Nevertheless, upon careful examination, we find that both the energy values and lifetimes of the levels scale exponentially with g; see Fig. 5. Numerically, we take the lifetime of a plateau of the oscillon τ to be the difference between the end of the plateau t_{end} and the start of the plateau t_{start}:

$$\tau = t_{\mathrm{start}} - t_{\mathrm{end}}. \tag{14}$$

For definiteness, t_{end} is taken to be the time when the energy decay rate $P(t)$ is ten times the $P(t)$ in the middle of the level plateau and the start t_{start} is taken to be the time

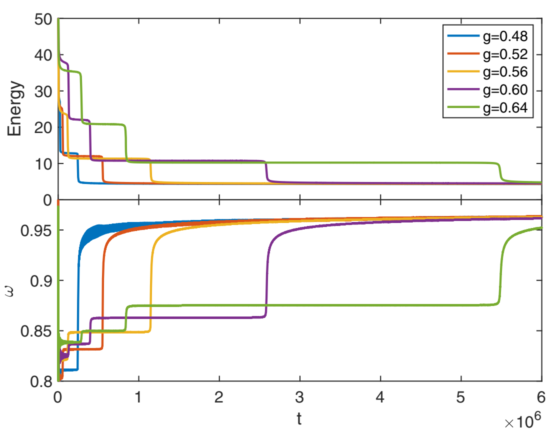

(a) 2+1D

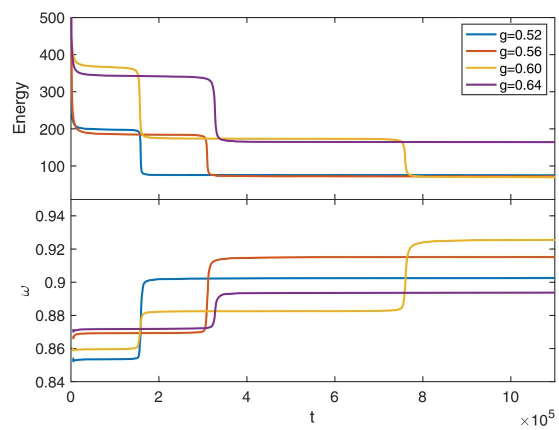

(b) 3+1D

FIG. 4. Dependence of the energy levels on the coupling g. The simulation setup is the same as in Fig. 1 except for the different values of g. While the energy levels of the oscillons are insensitive to the coupling, the lifespans of the levels increase with g. The frequency ω changes noticeably for different g, except for the first (most stable) level.

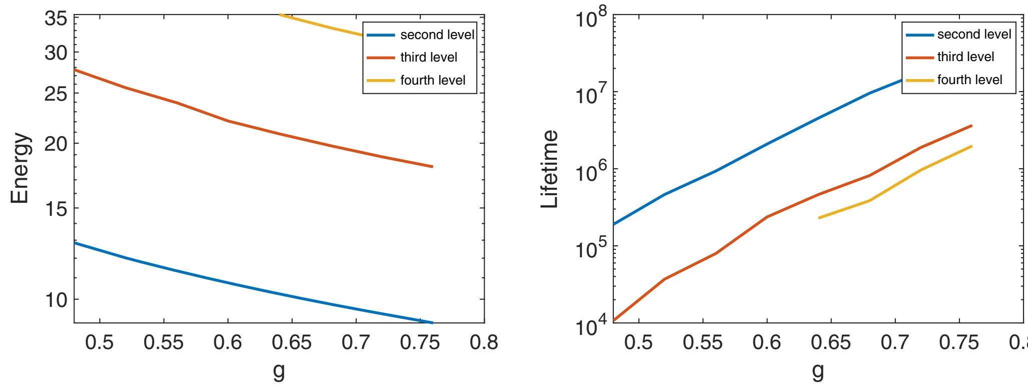

FIG. 5. Scaling behaviors of the energy values (left) and lifetimes (right) of the various levels on the coupling g. The nth level of the oscillon refers to the nth lowest energy level. The simulation setup is the same as in Fig. 1 except for the different values of g.

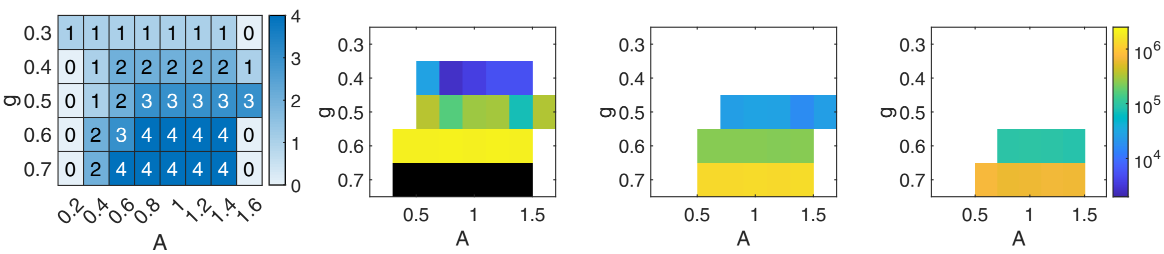

(a) (b) (c) (d)

FIG. 6. Dependence of the lifetime of each plateau on A and g. We set $a = 81$ and $\sigma = 90$ as a fiducial choice. Panel (a) shows the number of resolvable energy levels for the corresponding A and g. Panels (b), (c), and (d) show, respectively, how the lifetime of the second, third, and fourth level depends on A and g. The white regions are where the oscillon cannot have the relevant level, while the black regions show the cases where the level has not decayed when time reached $t = 5 \times 10^6$.

when the energy decay rate $P(t)$ is 10 times the $P(t)$ in the middle of the level plateau, where the energy decay rate can be simply computed by numerically evaluating $P(t) = |E(t + \mathrm{d}t) - E(t)|/\mathrm{d}t$.

In Fig. 6 we plot how the lifetime of each level changes for different A and g. As expected, we find that A has little effect on the lifetime as long as the relevant plateau forms in the evolution; the excess of the energy introduced by a larger A is simply shed away in the initial relaxation. The lifespans of the displayed energy levels also remain mostly unchanged upon varying other initial conditions. In Fig. 7 we explore how the energies and lifetimes of the third and fourth levels depend on the values of a and σ in Eq. (12). We see that they are not sensitive to the initial a and σ except near the boundary of the parameter space within which oscillons can form. This is a reflection of the fact that these energy levels are quasistable attractors of the system and justifies our sloppy choice of the initial configuration in Eq. (12), as the system will evolve to the attractor as long as it is within the attractor basin. For the spherical oscillons, the attractor basin is relatively sizable. It is possible to have higher-energy levels should one fine-tune the initial

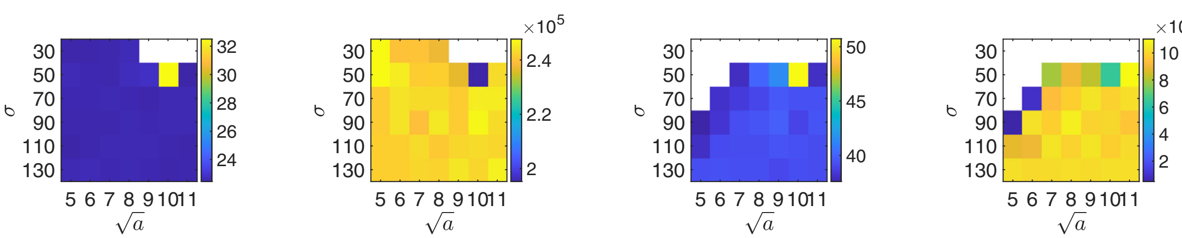

(a) Energy E of third level (b) Lifetime of third level (c) Energy E of fourth level (d) Lifetime of fourth level

FIG. 7. Dependence of energies and lifetimes of different levels on initial configurations. $A = 1.0$ and $g = 0.60$. We see that the energies and lifetimes are not sensitive to the initial a and σ except near the boundary of the parameter space where oscillons can form, meaning that these oscillons are some kind of attractors. The white regions are where the oscillon cannot have the relevant level.

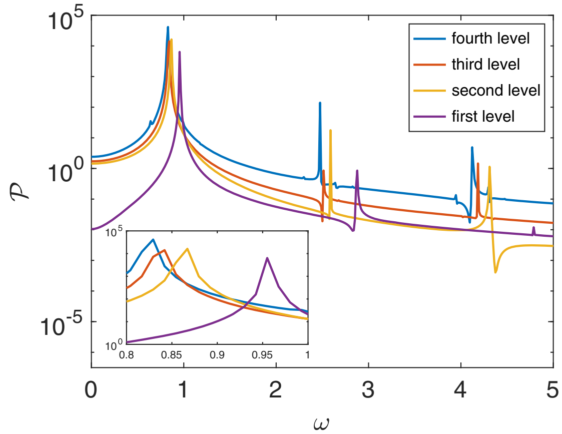

FIG. 8. Fourier spectra $\mathcal{P}$ of the scalar field at the center the spherical oscillon. The inset highlights the dominant peak near $\omega = 1$. The higher-frequency peaks are almost odd multiples of the base frequency near $\omega = 1$. The parameters for this plot are $g = 0.60$, $A = 1.0$, $a = 81$, and $\sigma = 90$, and the sampling times are $t_a = 2.1 \times 10^4, 1.75 \times 10^5, 1.75 \times 10^6, 3.9 \times 10^6$.

conditions, which is not vigorously pursued in this study. However, their lifetimes are much shorter.

It is also instructive to sample some Fourier spectra of the different energy levels of the oscillon. An example of these is shown in Fig. 8 where we plot the power spectra of the scalar field at a point in the center of the oscillon:

$$\mathcal{P} = |\tilde{\phi}(\omega, \mathbf{x}_0)|^2, \quad \text{where} \quad \tilde{\phi}(\omega, \mathbf{x}_0) = \int_{t_a}^{t_b} \mathrm{d}t e^{-i\omega t} \phi(t, \mathbf{x}_0), \tag{15}$$

where t_a, t_b are chosen to be within a flat part for each plateau of the oscillon and $t_b - t_a = 500$. It has a distinct peak structure: there is a dominant base frequency, which essentially determines the oscillation period of the oscillon, followed by smaller peaks around odd multiples of the base frequency. This justifies our semianalytical expansion scheme (6), which we will use in the next subsection. Turning the argument around, the reason why there are only odd multiples of the base frequency can be seen in the perturbative analysis (6); see the text below Eq. (11). Also, we see that the dominant peak frequency decreases as the energy of the level increases so that the most stable level, the first level, has the highest dominant peak frequency. The same is also true for the subleading peaks. Some kind of structural differences between the most stable level and the higher levels are also noticeable in both the frequencies and the peak powers, with the three higher levels staying more close to each other. This fits into the picture that the evolution of the oscillon is a process where its base frequency migrates to pass the limit of $\omega = 1$, where $\sqrt{1-\omega^2}$ changes from a real value to an imaginary value and the nature of the solution changes from oscillatory to dissipative. For example, the far field changes from $\phi \sim e^{-\sqrt{1-\omega^2}r}/r^{1/2}$ to $\phi \sim \cos(\sqrt{\omega^2-1}r)/r^{1/2}$, the latter allowing an energy outflow. Thus, the different energy plateaus can naturally appear in sequence during the entire lifetime of an excited oscillon.

B. Perturbative analysis

In this subsection we use the expansion scheme (6) to analyze some of the properties of the cascading oscillons explored with lattice simulations above. In particular, we semianalytically compute the lifespans of the energy levels.

The first order of business in the perturbative analysis using the expansion scheme (6) is to nonlinearly solve the background solution $\Phi_0(r)$. The approximation of the "background" oscillon with only a single mode is a rather crude one, and yet, as we will see, at least for our particular model this is rather a good approximation. In fact, to first-order approximation, we view the oscillon as consisting of this background plus a perturbative radiative field, which is the first excited A_n^l field (A_3^0 in this particular case).

With the expansion scheme (6), obtaining the background solution is fairly easy, as it only involves solving the following ODE:

$$\partial_r^2\Phi_0 + \frac{1}{r}\partial_r\Phi_0 + (\omega^2-1)\Phi_0 + \frac{3}{2}(\Phi_0)^3 - \frac{15}{8}g(\Phi_0)^5 = 0. \tag{16}$$

This can be easily done by a standard shooting method, shooting from near $r = 0$ to a large r, as mentioned in the last section. To the leading-order approximation, we simply estimate the energies of the oscillon levels with the background solution

$$\phi(t, r) \simeq \Phi_0(r) \cos\omega t. \tag{17}$$

To compare with the fully nonlinear solution of the last subsection, we set the initial parameters to be $A = 1$, $a = 81$, and $\sigma = 90$, and choose $g = 0.60$ as our fiducial model in this subsection. The Φ_0 profiles for a few different ω can be found in Fig. 9. A comparison between the energies of the oscillons computed from this perturbative approach ("perturbative energy") and from the nonlinear simulations in the last subsection ("nonlinear energy") can be found in Table I, showing good agreements between the two.

With the background established, to determine the lifetimes of the plateau levels, we need to estimate the decay rate or radiation emission rate of the oscillon. To this end, we include the perturbations or radiation fields A_n^0 in Eq. (6), which are sourced by the background field. As A_2^0 vanishes [cf. the text below Eq. (11)], the lowest-order radiation field is A_3^0. We only take this next-to-leading-order approximation. This is retrospectively justified by

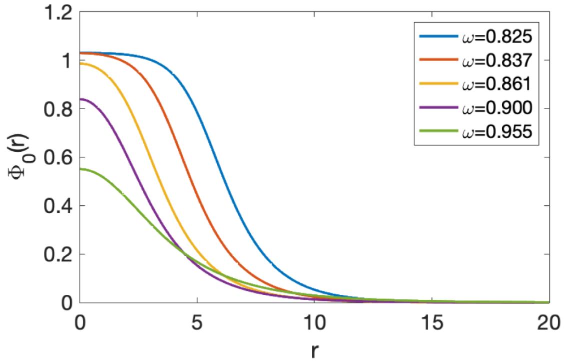

FIG. 9. Background profile $\Phi_0(r)$ for different ω. The parameters are the same as those in Fig. 1.

computing the quintuple contribution, or by simply inspecting the spectra in Fig. 8 and noticing that the power of the quintuple frequency is far weaker than that of the triple frequency. Therefore, the perturbation equation that needs solving is simply

$$\partial_r^2 A_3^0 + \frac{1}{r}\partial_r A_3^0 + (9\omega^2 - 1 - B_0^0)A_3^0 = C_3^0 + \mathcal{O}(A^2). \quad (18)$$

where B_0^0 and C_3^0 are defined in Eqs. (9) and (8) and contain sourcing and parametric enhancements from the background solution. As already mentioned in Sec. II, to numerically solve this ODE, because it falls off relatively slowly, one can use a shooting method that matches the asymptotical solution of this equation at a large r to improve the accuracy.

The decay rate of the oscillon can be obtained by computing at a large r the $0r$ component of the energy-momentum tensor of the scalar field, T_{0r}, which is the energy flux in the r direction. The background field Φ_0 goes like $e^{-\sqrt{1-\omega^2}r}/r^{1/2}$ for large r, so its contribution to T_{0r} can be safely neglected. To the leading-order approximation, we then have

$$T_{0r}(t, r\to\infty) = \partial_t[A_3^0(r)\cos(3\omega t)]\partial_r[A_3^0(r)\cos(3\omega t)]. \quad (19)$$

TABLE I. Comparison between the energy computed with only $\Phi_0(r)$ and the energy obtained from nonlinear simulations in the last subsection. The nth level refers to the nth energy plateau of the oscillon. The nonlinear energies are only approximate values because the energy does change slightly over the whole lifespan. The parameter setup is the same as in Fig. 1.

	Fourth level	Third level	Second level
Perturbative energy	39.67	23.22	11.75
Nonlinear energy	≈39	≈22	≈11

Asymptotically, $A_3^0(r)$ goes like $A_3^0(r) = A\cos(kr+\alpha)/r^{1/2}$, where $k = \sqrt{9\omega^2 - 1}$ and A and α are constants. [The value of A can be obtained by solving Eq. (18) and extracting $A = \max(r^{1/2}A_3^0)$ at large r around $r = 60$–100.] So, $T_{0r}(t,r)$ in the far field can be further approximated by

$$T_{0r}(t, r\to\infty) = \partial_t\left[\frac{A}{r^{1/2}}\cos(kr+\alpha)\cos(3\omega t)\right] \times \partial_r\left[\frac{A}{r^{1/2}}\cos(kr+\alpha)\cos(3\omega t)\right]. \quad (20)$$

To compute the decay rate, we only include the outgoing waves of the perturbative field A_3^0, which leads to

$$T_{0r}^{(\mathrm{out})}(t, r\to\infty) = \partial_t\left[\frac{A}{2r^{1/2}}\cos(kr - 3\omega t + \alpha)\right] \times \partial_r\left[\frac{A}{2r^{1/2}}\cos(kr - 3\omega t + \alpha)\right]. \quad (21)$$

Averaging over a few temporal oscillations and integrating over a circle at a large r, the energy decay rate of the oscillon (energy radiated away in a unit time by the oscillon) in the leading perturbative approximation is given by

$$P(\omega) = 2\pi r\langle T_{0r}^{(\mathrm{out})}(t, r\to\infty)\rangle_t = \frac{3\pi\omega k A^2}{4} = \frac{3\pi\omega k}{4}[\max(r^{\frac{1}{2}}A_3^0)]^2, \quad (22)$$

where the average $\langle\rangle$ is over time t. Therefore, for each frequency ω, we can obtain an energy decay rate. In terms of the energy decay rate, the reason for the existence of the multiple energy plateaus is because there are multiple frequencies (the frequencies of the levels identified in the last subsection) where the decay rate is exponentially suppressed. Having obtained the energy decay rate, one can then compute the lifespan of an excited oscillon level when it migrates from a lower frequency ω_1 to a higher frequency ω_2 by evaluating

$$\tau_{12} = \int_{\omega_1}^{\omega_2} \frac{\mathrm{d}E(\omega)/\mathrm{d}\omega}{P(\omega)}\mathrm{d}\omega, \quad (23)$$

where $E(\omega)$ is the energy of the background solution for a fixed ω, which can be obtained by integrating Eq. (16) for various ω. So, if we want to evaluate the lifetime of, say, the second energy plateau, we should let $\omega_1 < \omega_{\mathrm{second}} < \omega_2$, where ω_{second} is the dominant frequency of the second level. In this numerical evaluation, it is important to sample the frequencies close to the plateau frequency such as ω_{second} very finely, as the decay rates at those frequencies are significantly suppressed, which is precisely the reason to have excited oscillons at those frequencies. In Fig. 10 we see that the lifetimes of the excited oscillons computed from this

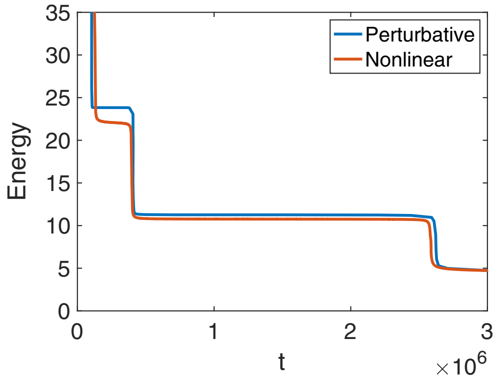

FIG. 10. Comparison of lifespans computed from the full nonlinear simulations and the leading perturbative analysis. The coupling is chosen to be $g = 0.6$ and the initial parameters are chosen to be $A = 1$, $a = 81$, and $\sigma = 90$.

perturbative approach match those of the previous full nonlinear simulations rather well.

To estimate the accuracy of the perturbative analysis, we compare the oscillon frequencies of the second and third energy levels between the nonlinear simulations and the perturbation results. The frequency ω_{p} from the perturbative analysis is extracted from the peak of the energy decay rate, and that of the corresponding simulation ω_{nl} is obtained by averaging over the duration of the level. The relative errors between the two are plotted in Fig. 11 for various g, with the other simulation parameters being $A = 1$, $a = 81$, and $\sigma = 90$. Since properly formed oscillons are insensitive to the initial condition parameters, it is sufficient to survey the error dependence on g. As shown in the figure, the relative errors are $\lesssim 1\%$ for a reasonably long-lived oscillon. A larger g corresponds to a longer-lived oscillon, in which case the perturbative analysis becomes more accurate; we see that the relative error

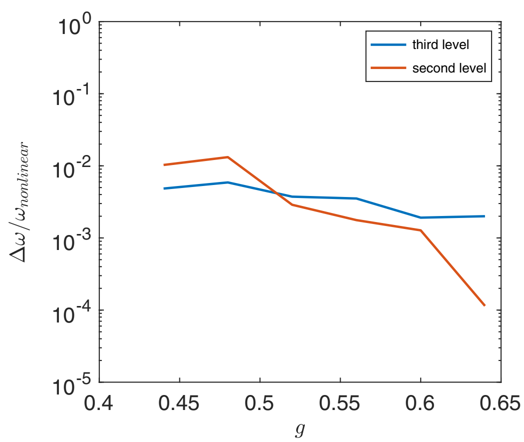

FIG. 11. Accuracy of the perturbative results, as compared to the nonlinear simulations, in terms of the oscillon frequencies for various g. The second and third levels refer to the energy levels defined in the previous figures.

reaches 0.01% for the lowest nontrivial level when $g \simeq 0.64$. When g reaches a threshold lower bound, which is around $g \simeq 0.4$, the configuration is too short lived to be regarded as an oscillon. All in all, as long as a long-lived oscillon can form, the perturbative method prevails and the higher orders of A_n^l ($n > 3$) are highly suppressed, having little influence on the decay of the oscillon.

Last, we would like to point out that the excited spherical oscillons we study in this paper can be intuitively viewed as a nodeless background plus a leading multinode perturbation, in terms of the expansion (6). Here, the node does conform to the usual meaning of a stationary point in the field's evolution. This underlies the difference between the energy density profile of the first plateau and those of the higher plateaus in Fig. 2. Solutions with a multinode background also exist, which are closer to the excited Q-balls studied in Refs. [74–78] and which we have also explicitly constructed, but the lifespans of these solutions are much shorter. For example, for the same setup as in Fig. 1, the solution with a one-node background only exists for a time duration of less than 400.

IV. MULTIPOLAR OSCILLONS

In the previous section we focused on the oscillons that are spherically symmetric. We uncovered a tower of excited spherical oscillons that have higher energies than the most quasistable oscillon. These excited oscillons have shorter lifespans as their energies increase, and can naturally emerge in succession from the evolution of a dense lump that is initially sufficiently close to these excited oscillons. In this section, we explore oscillons that are complex in a complementary direction, i.e., oscillons that are anisotropic. That is, we will see that there exist quasistable structures in real scalar theories that are multipolar. These are similar to spinning Q-balls [74,82–92]. One major difference is that, due to the realness of the scalar field in the current case, a multipolar oscillon must contain multiple multipoles, although one multipole can dominate its energy density. Also, we are unable to find the equivalence of charge-swapping Q-balls [79–81] in this real scalar case.

A. Dipolar oscillons

In the previous section, it was relatively straightforward to construct excited spherical oscillons, as they seem to be strong attractors that can easily arise from the relaxation of some approximate spherical configurations. This is also aided by the absorbing boundary condition which in the spherical case is quite efficient at eliminating the radiation emitted in the relaxation process. The numerical simulations were then checked to a good approximation by the semianalytical perturbative analysis. However, our strategy in this section will be slightly different, as the multipolar oscillons are less easier to construct. We prepare the initial configuration of a multipolar oscillon with the perturbative

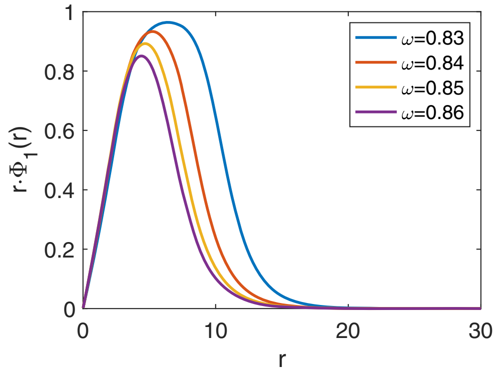

FIG. 12. Background profile $\Phi_1(r)$ for different ω. The coupling is chosen as $g = 0.64$.

method, although it is sufficient to include only the leading background solution, and then numerically simulate its evolution fully nonlinearly.

To construct an l_0-pole oscillon, we assume that the background field in Eq. (6) only has the l_0th multipole and does not have terms with $l < l_0$. For a dipolar oscillon, we have $l_0 = 1$ and the background field is given by

$$\phi(x) = \Phi_1(r) r \cos(\omega t - \theta) + \mathcal{O}(A), \tag{24}$$

which is rotating counterclockwise. We have factored out r such that Φ_1 has $\partial_r \Phi_1(r = 0) = 0$ as its boundary value at $r = 0$. The background field satisfies the following ODE:

$$\partial_r^2 \Phi_1 + \frac{3}{r}\partial_r \Phi_1 + \omega^2 \Phi_1 = \Phi_1 - \frac{3}{2} r^2 (\Phi_1)^3 + \frac{15}{8} g r^4 (\Phi_1)^5. \tag{25}$$

The $r\Phi_1$ profiles for a few different ω are shown in Fig. 12. As already anticipated in the factorization of $r\Phi_1$, the background field must vanish linearly in the center for the dipole. Inputting these background multipole solutions as the initial conditions in Cartesian simulations, we find rotating dipolar solutions. Typical time evolutions of the field values of the field and the energy density are shown in Fig. 13. We see that the field rotates at the same period as the field's dominant oscillation, while the energy density rotates at half of the period of the field's dominant oscillation. The energy density vanishes both in and far away from the center of the oscillon.

However, we are unable to construct a nonrotating dipolar oscillon. Nonrotating initial setups would only lead to two repelling oscillons, as closely placed oscillating lumps in antiphase repel each other [79]. This is different from a complex scalar field with a U(1) symmetry, where it is actually possible to have nonrotating multipolar solutions, dubbed charge-swapping Q-balls [79]. In that case, due to the luxury of a complex field that has two real components, a Q-ball can be roughly thought of as two oscillons for the two real components, respectively, which gives rise to dipolar configurations where the dominant oscillons are actually in phase (for a real scalar, they can only be in antiphase). This provides attractive forces between the lumps and allows nonrotating dipolar Q-balls to form.

As perhaps naturally expected, the lifespan of the dipolar oscillon is less than that of the spherical oscillons, with all parameters chosen equal; see Fig. 14. Recall that for the same coupling constant g, we have not seen the most stable oscillon decay in our simulations and, from Fig. 6, we see that even the lifespan of the second or third energy level of the spherical oscillon is significantly longer than that of the dipolar oscillon. Additionally, the energy of a dipolar oscillon is slightly higher than the highest-level spherical oscillon we are able to construct. In Fig. 14 we also see that what has been constructed is not a perfect dipole, with the distance between the peak values of the field oscillating slightly with time, especially in the first half of its evolution. This is probably partly due to our method of construction which only makes use of the zeroth-order approximation with the background field. However, the dipolar oscillon is not a factorizable solution, so some level of multipole mixing is expected. The oscillation does subside in a slow relaxation process. In our simulations, the dipolar oscillon always ends with two lumps flying away from each other, as we can see in Fig. 14.

We can also utilize the higher-order perturbative analysis to estimate the decay rate of the dipolar oscillon, as we did in Sec. III B. Again, since A_2^2 vanishes, the lowest-order radiation field is A_3^3, whose equation of motion is given by

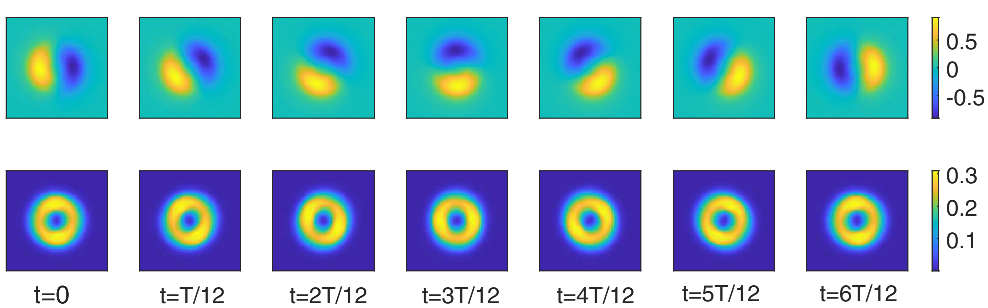

FIG. 13. Evolution of the dipolar oscillon. The top row is the evolution of the ϕ field and the bottom row is the evolution of the energy density. The rotation period of the field is T, while that of the energy density is $T/2$, where $T = 2\pi/\omega$ [see Eq. (24) for the definition of ω]. Both rotate counterclockwise in our initial setup. The coupling is chosen to be $g = 0.64$.

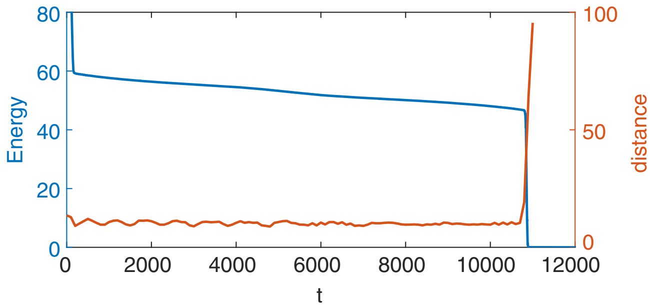

FIG. 14. Evolution of the energy and distance between the dipole peaks for a dipolar oscillon. The dipolar oscillon disintegrates into two lumps flying away from each other at its demise. The parameter choices are the same as those in Fig. 13.

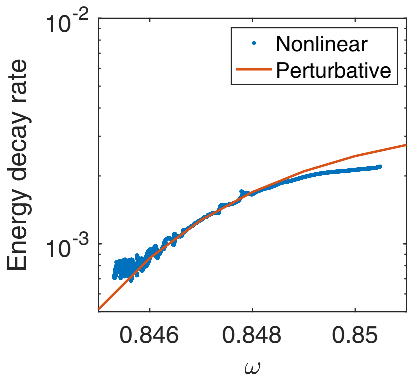

FIG. 15. Comparison of the decay rates between the perturbative approach and the nonlinear simulations for the dipolar oscillon for a section of frequencies. The parameter choices are the same as those in Fig. 13.

$$\partial_r^2 A_3^3 + \frac{7}{r}\partial_r A_3^3 + (9\omega^2 - 1 - B_0^0)A_3^3 = \frac{C_3^3}{r^3} + \mathcal{O}(A^2), \quad (26)$$

where $C_3^3(r)$ and $B_0^0(r)$ are defined in Eqs. (9) and (8). Going through similar steps as in the spherical case, we can get that the decay rate of the dipolar oscillon is given by

$$P(\omega) = 2\pi r \langle T_{0r}^{(\mathrm{out})}(t, r\to\infty, \theta)\rangle_{t,\theta} = \frac{3\pi\omega k}{8}[\max(r^{\frac{1}{2}}A_3^3)]^2, \quad (27)$$

where here the average $\langle\rangle$ is over the time t and angle θ. We can compare the decay rates from this perturbative approach with those computed from the nonlinear simulations, as shown in Fig. 15 for a range of frequencies. This range of frequencies corresponds exactly to the evolution of the dipole oscillon in Fig. 14 where the distance between the peaks is stabilized.

It is also instructive to see the oscillation patterns of the field at different parts of the dipolar oscillon. In Fig. 16 we plot the Fourier power spectra of the field at the points $r = 4.9$ and $r = 81.9$. (The dipolar oscillon is nonspherical, but its profile is spherically symmetric, with the difference in the different directions being only in the phase.) We can clearly see that the base frequency dominates the spectrum near the center of the spinning oscillon, while it is the third multiple of the base ω that dominates far away from the center. This justifies the approximation we use in the perturbative analysis above using a background field with a base frequency and a radiation field with three multiples of the base.

We would like to stress that the stability of dipolar oscillons is rather sensitive to initial conditions. This is

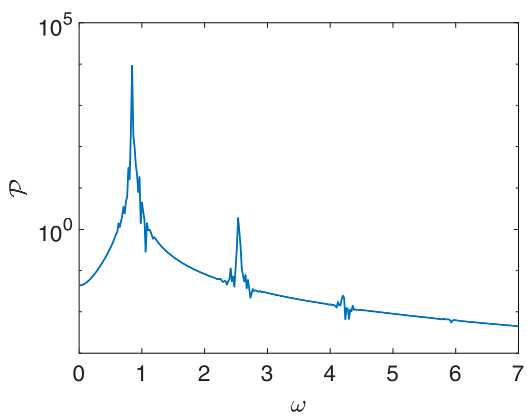

(a) Power spectrum of $\phi(t, r = 4.9)$.

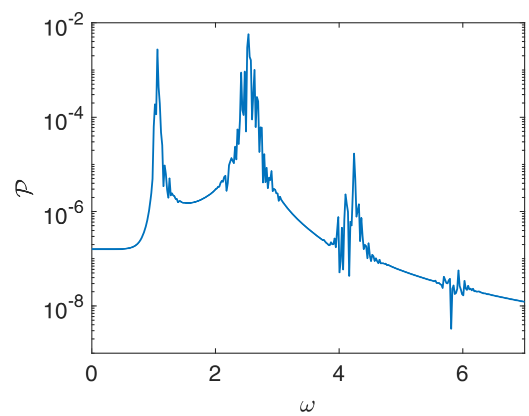

(b) Power spectrum of $\phi(t, r = 81.9)$

FIG. 16. Fourier power spectra of the scalar field at two representative points. We can see that the base frequency dominates the spectrum near the center of the spinning oscillon, while it is the third multiple of the base ω far away from the center. The parameter choices are the same as those in Fig. 13.

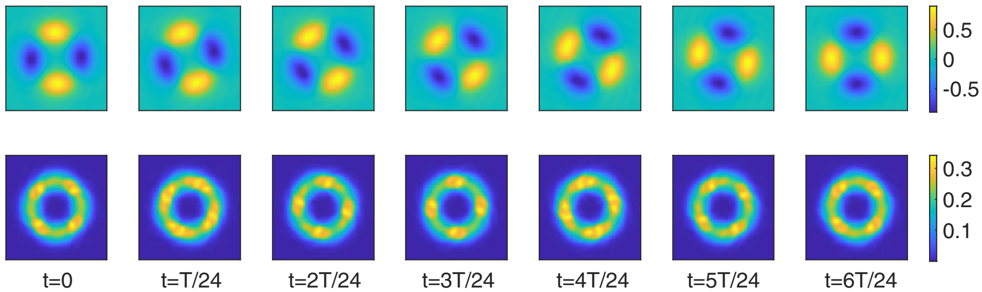

FIG. 17. Evolution of the quadrupolar oscillon. The top row is the evolution of the ϕ field and the bottom row is the evolution of the energy density. The rotation period of the ϕ field is denoted as T, while the rotation period of the energy density is $T/2$, where $T = 2\pi/\omega$ [see Eq. (28) for the definition of ω]. The coupling is chosen to be $g = 0.64$.

different from the case of spherical/monopole oscillons, whose ability to form is insensitive to the initial configurations. Therefore, in order to construct a dipolar oscillon, it is essential to solve the equation of motion of the background field (25) accurately and use it as the initial input. In other words, the "attractor basin" of the dipolar oscillon is much smaller than the monopolar oscillon. Also, the end state of a dipolar oscillon is the dissipation of the dipolar oscillon. For the case of a spherical oscillon, its evolution can be tracked in the frequency space where the oscillon's frequency increases with time until the frequency reaches the upper limit, which is the mass of the field, and then the field oscillation is no longer supported, leading to the oscillon disintegrating via dissipation. However, for the dipolar oscillon, the end state is when the attraction between the lumps of the dipole can not support its rotation, and the two lumps fly away from each other. However, both processes happen very quickly.

B. Higher-multipole oscillons

It is also possible to construct higher-multipole oscillons by preparing the initial conditions with the leading background field solutions. For example, for the case of $l_0 = 2$, we only need to consider the background

$$\phi(t, r, \theta) = \Phi_2(r) r^2 \cos(\omega t - 2\theta) + \mathcal{O}(A), \qquad (28)$$

where Φ_2 satisfies the ODE

$$\partial_r^2 \Phi_2 + \frac{5}{r}\partial_r \Phi_2 + \omega^2 \Phi_2 = \Phi_2 - \frac{3}{2} r^4 (\Phi^2)^3 + \frac{15}{8} g r^8 (\Phi_2)^5. \qquad (29)$$

This ODE again can be solved by a shooting method and, using it as the initial condition, the initial configuration will quickly relax to a quadrupolar oscillon, as shown in Fig. 17. Quadrupoles usually have shorter lifetimes than dipoles. Taking $g = 0.64$ as an example, dipoles have lifetimes on the scale of 10^4, while quadrupole lifetimes are on the scale of 10^3. Similar to the dipoles, for the quadrupoles we have observed so far, the final decay process is still disintegration via separation.

The lifetimes of even higher-multipole oscillons are much shorter. By again preparing them with the background field method, we find that the sextuple oscillon ($l_0 = 3$) only lives for a duration of about 10^2, which is just dozens of periods of the underlying field oscillations. If we plot the typical lifetime scales of different multipolar oscillons, as shown in Fig. 18, we see that the lifetime scale decreases exponentially with the number of the multipole (l_0). Of course, the lifespans of multipolar oscillons are expected to depend on the potential, as they do for the charge-swapping Q-balls [80,81]. While the above results are quite general in the sense that the polynomial potential we use is the leading approximation in the presence of a rapidly converging Taylor expansion, some other potentials such as the logarithmic effective potential commonly arising from loop corrections may lead to excited oscillons with longer lifespans. We leave exploration of this for future work.

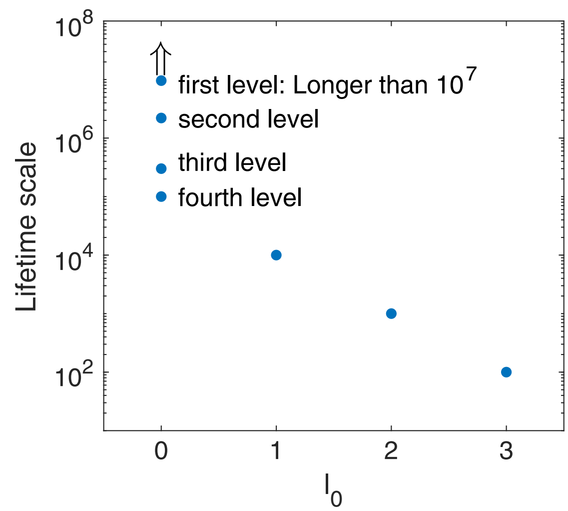

FIG. 18. Lifetime scales for leading multipolar oscillons (for coupling $g = 0.64$). l_0 refers to the multipole of the dominant mode. For the spherical ones ($l_0 = 0$), we plot all four energy levels we found in the last section.

V. SUMMARY AND OUTLOOK

In this paper we investigated two types of excited oscillons. The first type is spherically symmetric oscillons with higher energies. As its energy increases, such an excited oscillon has an increasingly lower oscillation frequency and shorter lifetime than the unexcited one. They are characterized by increasingly more (approximate) nodes in their radial profiles. We also preliminarily surveyed the parameter space for their lifetimes numerically. The lifetimes can also be estimated semianalytically by approximating the oscillon with a factorizable background with a fixed frequency plus radiation fields with higher-multiple frequencies. It is often sufficient to only include the leading radiation field. One interesting feature is that, starting from a higher-energy oscillon, it will cascade through all of the lower-energy phases before the oscillon dissipates, and the different phases of the oscillon are connected by rapid bursts of energy radiation.

The existence of these higher-energy spherical oscillons may also be seen by computing the decay rate of the oscillon, by which one finds that there are oscillation frequencies where the rate is exponentially suppressed, leading to these metastable oscillons. Flipping the argument, the underlying reason for the existence of the suppressed decay rates is that there are approximate multinode oscillon solutions to the equations of motion. The cascading feature of its evolution might also be expected, as the evolution of the oscillon is basically a process where the dominant frequency of the oscillon slowly increases to higher values until reaching the upper limit when the oscillon quickly disintegrates.

The second type of metastable oscillons we uncovered are those with higher multipoles. Nonspherical structures for Q-balls, which are cousins of oscillons, have been investigated previously. Similar to the unexcited oscillon, these multipolar oscillons are also not factorizable, and there are necessarily many multipoles involved. Nevertheless, typically, one multipole will dominate, making the overall behavior similar to a multipolar Q-ball. As the multipolar oscillons are more sensitive to the initial conditions than the spherical ones, it is essential that one prepares the initial configuration by the semianalytical method so as to numerically construct these oscillons.

The multipolar oscillons we obtained are the counterparts of the spinning Q-balls [74], in which the field profile rotates in one direction. However, we were unable to construct the counterparts of the charge-swapping Q-balls [79]. The difference again originates from the fact that for oscillons we have only a single component scalar field compared with a complex field for Q-balls, so a multipolar oscillon necessarily has multiple multipoles. For such configurations, aligning the opposite rotating configurations cannot be achieved for all of the multipoles simultaneously.

The lifespans of the multipolar oscillons are significantly shorter than those spherical excited states. In particular, for our polynomial model, we only found reasonably long-lived oscillons up to the sextuple ones in $2+1$D ($l_0 = 3$, with the multipole number l_0 here referring to the dominant mode), which only live for tens of oscillations. However, multipolar oscillons may be obtainable for other potentials such as logarithmic ones, as we have seen very long-lived charge-swapping Q-balls in a logarithmic potential [81].

As mentioned in the Introduction, the current cosmological data indicate that the inflaton potential is very flat [43], which can lead to an oscillon-dominated epoch after inflation [52]. The oscillons arise from the fragmentation of the inflaton condensate in the preheating period, induced by parametric resonance, which is accompanied by a stochastic gravitational-wave background [58]. This is a rather random process, which suggests that the initially formed oscillons are unlikely to be in the ground state, and the excited oscillons will go through an energy-cascading process (or in favorable circumstances higher-multipole oscillons may form), as depicted here. In the watershed moments where the energy of the oscillon steps down in the levels, a burst of energy will be produced. A more interesting scenario is when oscillons are produced at a lower energy scale from some preheating-like mechanism, in which case the gravitational-wave background might be observable by the gravitational-wave detectors [61]. Indeed, particle physics models such as supersymmetry accommodate many scalars with flat potentials, and field condensates can form thanks to the Hubble expansion [94,95], which gives rise to a preheating-like process well below the inflation scale. It is interesting to investigate how the energy cascading of the oscillons affects the thermal history and gravitational-wave background around the reheating period and in late cosmic epochs, which is left for future work.

On a different note, oscillons are a phenomenon that can be generated in laboratory settings [71–73], in which case it would be interesting to first observe the energy cascading and the higher multipoles in laboratories, and then explore possible applications of these novel nonlinear phenomena.

ACKNOWLEDGMENTS

We would like to thank Xiao-Xiao Kou, Anzhuoer Li, and Paul Saffin for helpful discussions. S.-Y. Z. acknowledges support from the Fundamental Research Funds for the Central Universities under Grant No. WK2030000036, from the National Natural Science Foundation of China under Grant Nos. 12075233 and 12247103, and from the National Key R&D Program of China under grant No. 2022YFC220010.

APPENDIX A: NUMERICAL CODES

As mentioned, we make use of two separate codes to run the nonlinear simulations in this paper: a spherical grid code and a Cartesian code. Both are endowed with absorbing boundary conditions, as we are interested in the lifetimes of the oscillons.

1. Spherical code

For the spherical code, symmetric boundary conditions are introduced at the origin and absorbing boundary conditions are introduced in the far field. For our purposes, it is sufficient to use a grid with radius $R = 128$, and to choose the radial step size to be $dr = 0.25$ and the temporal step size to be $dt = 0.01dr$. We use the Runge-Kutta fourth-order method to evolve it temporally. The Courant-Friedrichs-Lewy (CFL) factor is chosen to be relatively small so as to improve convergence, but it is still at least 2 orders of magnitude faster than the equivalent Cartesian code.

For the spherical code, the absorbing boundary condition can be implemented as follows. First, note that the equation of motion in $d+1$ dimensions in the far field (large r) is given by

$$\frac{\partial^2\phi}{\partial t^2} - \frac{\partial^2\phi}{\partial r^2} - \frac{d-1}{r}\frac{\partial\phi}{\partial r} + \phi = \mathcal{O}(\phi^2), \tag{A1}$$

so the outgoing wave solution with frequency ω is given by $\phi \simeq \exp[i(\sqrt{\omega^2-1}r - \omega t)]/r^{(d-1)/2}$ at large r. For waves whose frequencies are much greater than 1, it can be approximated by $\phi \simeq \exp[i(\omega r - \frac{1}{2\omega}r - \omega t)]/r^{(d-1)/2}$. Such outgoing waves are solutions of the differential equation

$$\left(\partial_t\partial_r + \partial_t^2 + \frac{1}{2} + \frac{d-1}{2r}\partial_t\right)\phi = 0, \tag{A2}$$

while the ingoing waves are not. Therefore, we can implement this as the boundary conditions at large r, which will efficiently absorb outgoing waves whose frequencies are larger than the mass of the field.

2. Cartesian code

The Cartesian code is used to cross-check with the spherical code in the study of cascading oscillons and to run simulations for multipolar oscillons. The code is parallelized in the framework of LATfield2 [96]. The spatial derivatives in the equation of motion are approximated by fourth-order finite differences and the time evolution is performed using the Runge-Kutta fourth-order method. We make use of Higdon's absorbing boundary conditions [97,98] to absorb outgoing waves and reduce unphysical wave reflections at the boundary. These conditions can absorb waves with multiple fixed phase velocities completely and also absorb waves with a broad range of mismatched phase velocities rather well, provided the parameters of the fixed phase velocities are chosen judiciously. A second-order Higdon's condition implemented at the boundaries in the x^i direction is

$$\left(\frac{\partial^2}{\partial t^2} \pm (c_1+c_2)\frac{\partial}{\partial x^i\partial t} + c_1c_2\frac{\partial^2}{\partial(x^i)^2}\right)\phi\bigg|_{x^i=a} = 0, \tag{A3}$$

where $+(-)$ indicates the condition to be applied at the upper (lower) x^i boundary and a is the location of the boundary. The c_j's are tunable constants, which should be chosen to be close to the phase velocities of the far-field waves. In our case, we simply set $c_1 = c_2 = 1$. See Ref. [80] for more details. For the other numerical setup, the spatial grid is chosen to have 1024×1024 sites and the physical spacing between adjacent sites is $dx = 0.2$. The time step is chosen to be $dt = 0.02$ to satisfy the CFL condition.

APPENDIX B: DECOUPLING BETWEEN DIFFERENT SETS OF A_n^l MODES

In this appendix, we analyze the structure of the perturbative equations of motion and separate out the perturbative modes that are sourced by the background from those that are decoupled from the background. These decoupled modes include the A_n^l modes with negative l.

Consider a counterclockwise-spinning background field Φ_{l_0} ($l_0 > 0$) supplemented with both positive and negative l perturbative fields A_n^l,

$$\begin{aligned}\phi(t,r,\theta) &= \Phi_{l_0}(r)r^{l_0}\cos(\omega t - l_0\theta)\\ &\quad + \sum_{n>1,|l|>l_0} A_n^l(r)r^{|l|}\cos(n\omega t - l\theta).\end{aligned} \tag{B1}$$

The perturbation equation of motion takes the following form:

$$\begin{aligned}&\partial_r^2A_n^l + \frac{2|l|+1}{r}\partial_rA_n^l + (n^2\omega^2 - 1 - B_0^0)A_n^l - \frac{C_n^l}{r^{|l|}}\\ &\quad = \frac{1}{2r^{|l|}}\sum_{j=2}^{\infty}B_j^{jl_0}\left(r^{|l+jl_0|}A_{n+j}^{l+jl_0} + r^{|l-jl_0|}A_{n-j}^{l-jl_0}\right),\end{aligned} \tag{B2}$$

where C_n^l and B_n^l are defined by Eqs. (8) and (9), respectively. Relabeling l as $l = nl_0 + k$, where k is an integer with $|nl_0+k| > l_0$, we can rewrite the above equation as

$$\partial_r^2A_n^{nl_0+k} + \frac{2|nl_0+k|+1}{r}\partial_rA_n^{nl_0+k} + (n^2\omega^2 - 1 - B_0^0)A_n^{nl_0+k} - \frac{C_n^{nl_0+k}}{r^{|nl_0+k|}} \tag{B3}$$

$$= \frac{1}{2r^{|nl_0+k|}}\sum_{j=2}^{\infty}B_j^{jl_0}\left(r^{|(n+j)l_0+k|}A_{n+j}^{(n+j)l_0+k} + r^{|(n-j)l_0+k|}A_{n-j}^{(n-j)l_0+k}\right). \tag{B4}$$

An immediate observation is that the above set of equations separate into a number of subsets of equations that are labeled by k, with the subsets decoupled from each other. In other words, the $A_n^{nl_0+k}$ modes with the same k are coupled, while the $A_n^{nl_0+k}$ modes with different k are decoupled from each other. Also, $C_n^{nl_0+k}$ is nonzero only when $k = 0$. That is, all of the $A_n^{nl_0+k}$ modes with nonzero k are unsourced; the $A_n^{nl_0+k}$ with the same nonzero k satisfies a system of unsourced/homogeneous linear ODEs, and therefore these modes are not excited by our background field Φ_{l_0}. These unsourced modes include the modes where A_n^l has $l < 0$.

APPENDIX C: CONVERGENCE STUDY OF CASCADING OSCILLONS

In Sec. III we make use of a spherical code to simulate cascading oscillons, which speeds up exploration of the parameter space. The spherical code also allows implementation of more efficient absorbing boundary conditions, but has the disadvantage of neglecting nonspherical modes, which may contribute to the decay of the oscillons. The generic expectation is that for a spherical oscillon the dominant decay mode is the monopole mode. In this appendix, we verify that this is indeed the case by comparing a typical evolution in the spherical simulation with the corresponding Cartesian simulations.

Figure 19 shows the evolution of a typical cascading oscillon. We see that the lifetimes of the levels of the oscillons in the $(2 + 1\mathrm{D})$ Cartesian code converge to that in the spherical code as the accuracy increases. Quantities such as lifetimes are more difficult to determine numerically than quantities that can be measured at one time instance, as numerical errors can accumulate with time in the former case. Figure 19 highlights that the accuracy in the Cartesian code needs to be higher than that in the spherical code to converge to the actual result. For a comparison of computing resources needed for the matched runs in Fig. 19 (the spherical code and the most accurate Cartesian code), the Cartesian code uses a grid of 1024×1024 points and requires more than 200 wall-clock hours using 16 threads to reach $t = 1.4 \times 10^5$, while the spherically symmetric code only needs a 256×2 grid and takes about 3 wall-clock hours using 16 threads to reach the same physical time, which is the reason we used the spherical code to perform the parameter space survey. This justifies the use of the spherical code to analyze the properties of the spherical oscillons.

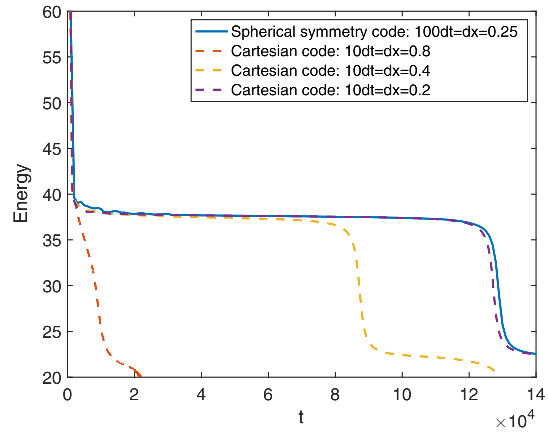

FIG. 19. Validation of the spherical code with Cartesian simulations. The spherical code is used to map the parameter spaces of cascading oscillons. We choose $g = 0.60$.

[1] G. Derrick, J. Math. Phys. (N.Y.) **5**, 1252 (1964).
[2] R. Friedberg, T. D. Lee, and A. Sirlin, Phys. Rev. D **13**, 2739 (1976).
[3] S. R. Coleman, Nucl. Phys. **B262**, 263 (1985); **B269**, 744 (A) (1986).
[4] T. D. Lee and Y. Pang, Phys. Rep. **221**, 251 (1992).
[5] I. L. Bogolyubsky and V. G. Makhankov, Pis'ma Zh. Eksp. Teor. Fiz. **24**, 15 (1976), https://inspirehep.net/literature/114626.
[6] E. J. Copeland, M. Gleiser, and H. R. Muller, Phys. Rev. D **52**, 1920 (1995).
[7] E. P. Honda and M. W. Choptuik, Phys. Rev. D **65**, 084037 (2002).
[8] A. B. Adib, M. Gleiser, and C. A. S. Almeida, Phys. Rev. D **66**, 085011 (2002).
[9] E. Farhi, N. Graham, V. Khemani, R. Markov, and R. Rosales, Phys. Rev. D **72**, 101701 (2005).
[10] M. Hindmarsh and P. Salmi, Phys. Rev. D **74**, 105005 (2006).
[11] G. Fodor, P. Forgacs, P. Grandclement, and I. Racz, Phys. Rev. D **74**, 124003 (2006).
[12] P. M. Saffin and A. Tranberg, J. High Energy Phys. 01 (2007) 030.
[13] N. Graham, Phys. Rev. Lett. **98**, 101801 (2007); **98**, 189904(E) (2007).
[14] M. Hindmarsh and P. Salmi, Phys. Rev. D **77**, 105025 (2008).
[15] G. Fodor, P. Forgacs, Z. Horvath, and A. Lukacs, Phys. Rev. D **78**, 025003 (2008).
[16] M. Gleiser and D. Sicilia, Phys. Rev. Lett. **101**, 011602 (2008).
[17] G. Fodor, P. Forgacs, Z. Horvath, and M. Mezei, Phys. Lett. B **674**, 319 (2009).
[18] M. Gleiser and D. Sicilia, Phys. Rev. D **80**, 125037 (2009).

[19] M. P. Hertzberg, Phys. Rev. D **82**, 045022 (2010).
[20] P. Salmi and M. Hindmarsh, Phys. Rev. D **85**, 085033 (2012).
[21] E. A. Andersen and A. Tranberg, J. High Energy Phys. 12 (2012) 016.
[22] M. A. Amin, Phys. Rev. D **87**, 123505 (2013).
[23] V. Achilleos, F. K. Diakonos, D. J. Frantzeskakis, G. C. Katsimiga, X. N. Maintas, E. Manousakis, C. E. Tsagkarakis, and A. Tsapalis, Phys. Rev. D **88**, 045015 (2013).
[24] P. M. Saffin, P. Tognarelli, and A. Tranberg, J. High Energy Phys. 08 (2014) 125.
[25] R. A. C. Correa, R. da Rocha, and A. de Souza Dutra, Phys. Rev. D **91**, 125021 (2015).
[26] M. Kawasaki, F. Takahashi, and N. Takeda, Phys. Rev. D **92**, 105024 (2015).
[27] K. Mukaida, M. Takimoto, and M. Yamada, J. High Energy Phys. 03 (2017) 122.
[28] T. Ikeda, C.-M. Yoo, and V. Cardoso, Phys. Rev. D **96**, 064047 (2017).
[29] S. Antusch, F. Cefala, S. Krippendorf, F. Muia, S. Orani, and F. Quevedo, J. High Energy Phys. 01 (2018) 083.
[30] M. Gleiser, M. Stephens, and D. Sowinski, Phys. Rev. D **97**, 096007 (2018).
[31] J. Sakstein and M. Trodden, Phys. Rev. D **98**, 123512 (2018).
[32] M. Ibe, M. Kawasaki, W. Nakano, and E. Sonomoto, J. High Energy Phys. 04 (2019) 030.
[33] S. Antusch, F. Cefalà, and F. Torrentí, J. Cosmol. Astropart. Phys. 10 (2019) 002.
[34] M. Ibe, M. Kawasaki, W. Nakano, and E. Sonomoto, Phys. Rev. D **100**, 125021 (2019).
[35] P. Dorey, T. Romanczukiewicz, and Y. Shnir, Phys. Lett. B **806**, 135497 (2020).
[36] D. Bazeia, A. R. Gomes, K. Z. Nobrega, and F. C. Simas, Phys. Lett. B **803**, 135291 (2020).
[37] G. Fodor, Ph.D. thesis, Wigner RCP, Budapest, 2019, arXiv:1911.03340.
[38] Z. Nazari, M. Cicoli, K. Clough, and F. Muia, J. Cosmol. Astropart. Phys. 05 (2021) 027.
[39] F. Van Dissel and E. I. Sfakianakis, Phys. Rev. D **106**, 096018 (2022).
[40] J. Olle, O. Pujolas, and F. Rompineve, J. Cosmol. Astropart. Phys. 09 (2021) 015.
[41] D. Cyncynates and T. Giurgica-Tiron, Phys. Rev. D **103**, 116011 (2021).
[42] B. C. Nagy and G. Takacs, Phys. Rev. D **104**, 056033 (2021).
[43] Y. Akrami *et al.* (Planck Collaboration), Astron. Astrophys. **641**, A10 (2020).
[44] M. Broadhead and J. McDonald, Phys. Rev. D **72**, 043519 (2005).
[45] M. Gleiser, Int. J. Mod. Phys. D **16**, 219 (2007).
[46] N. Graham and N. Stamatopoulos, Phys. Lett. B **639**, 541 (2006).
[47] E. Farhi, N. Graham, A. H. Guth, N. Iqbal, R. R. Rosales, and N. Stamatopoulos, Phys. Rev. D **77**, 085019 (2008).
[48] M. A. Amin and D. Shirokoff, Phys. Rev. D **81**, 085045 (2010).
[49] M. A. Amin, arXiv:1006.3075.
[50] M. A. Amin, R. Easther, and H. Finkel, J. Cosmol. Astropart. Phys. 12 (2010) 001.
[51] M. Gleiser, N. Graham, and N. Stamatopoulos, Phys. Rev. D **83**, 096010 (2011).
[52] M. A. Amin, R. Easther, H. Finkel, R. Flauger, and M. P. Hertzberg, Phys. Rev. Lett. **108**, 241302 (2012).
[53] S. Antusch and S. Orani, J. Cosmol. Astropart. Phys. 03 (2016) 026.
[54] K. D. Lozanov and M. A. Amin, Phys. Rev. D **97**, 023533 (2018).
[55] J.-P. Hong, M. Kawasaki, and M. Yamazaki, Phys. Rev. D **98**, 043531 (2018).
[56] X.-X. Kou, C. Tian, and S.-Y. Zhou, Classical Quantum Gravity **38**, 045005 (2021).
[57] Y. Sang and Q.-G. Huang, Phys. Lett. B **823**, 136781 (2021).
[58] S.-Y. Zhou, E. J. Copeland, R. Easther, H. Finkel, Z.-G. Mou, and P. M. Saffin, J. High Energy Phys. 10 (2013) 026.
[59] S.-Y. Zhou, J. Cosmol. Astropart. Phys. 06 (2015) 033.
[60] S. Antusch, F. Cefala, and S. Orani, Phys. Rev. Lett. **118**, 011303 (2017); **120**, 219901(E) (2018).
[61] J. Liu, Z.-K. Guo, R.-G. Cai, and G. Shiu, Phys. Rev. Lett. **120**, 031301 (2018).
[62] S. Antusch, F. Cefala, and S. Orani, J. Cosmol. Astropart. Phys. 03 (2018) 032.
[63] E. Cotner, A. Kusenko, and V. Takhistov, Phys. Rev. D **98**, 083513 (2018).
[64] M. A. Amin, J. Braden, E. J. Copeland, J. T. Giblin, C. Solorio, Z. J. Weiner, and S.-Y. Zhou, Phys. Rev. D **98**, 024040 (2018).
[65] K. D. Lozanov and M. A. Amin, Phys. Rev. D **99**, 123504 (2019).
[66] Y. Sang and Q.-G. Huang, Phys. Rev. D **100**, 063516 (2019).
[67] E. Cotner, A. Kusenko, M. Sasaki, and V. Takhistov, J. Cosmol. Astropart. Phys. 10 (2019) 077.
[68] T. Hiramatsu, E. I. Sfakianakis, and M. Yamaguchi, J. High Energy Phys. 03 (2021) 021.
[69] X.-X. Kou, J. B. Mertens, C. Tian, and S.-Y. Zhou, Phys. Rev. D **105**, 123505 (2022).
[70] K. D. Lozanov and V. Takhistov, Phys. Rev. Lett. **130**, 181002 (2023).
[71] P. B. Umbanhowar, F. Melo, and H. L. Swinney, Nature (London) **382**, 793 (1996).
[72] O. Lioubashevski, Y. Hamiel, A. Agnon, Z. Reches, and J. Fineberg, Phys. Rev. Lett. **83**, 3190 (1999).
[73] H. Arbell and J. Fineberg, Phys. Rev. Lett. **85**, 756 (2000).
[74] M. S. Volkov and E. Wohnert, Phys. Rev. D **66**, 085003 (2002).
[75] M. Mai and P. Schweitzer, Phys. Rev. D **86**, 096002 (2012).
[76] A. Y. Loginov and V. V. Gauzshtein, Phys. Rev. D **102**, 025010 (2020).
[77] Y. Almumin, J. Heeck, A. Rajaraman, and C. B. Verhaaren, Eur. Phys. J. C **82**, 801 (2022).
[78] P. Klimas, N. Sawado, and S. Yanai, Phys. Rev. D **105**, 085004 (2022).
[79] E. J. Copeland, P. M. Saffin, and S.-Y. Zhou, Phys. Rev. Lett. **113**, 231603 (2014).

[80] Q.-X. Xie, P. M. Saffin, and S.-Y. Zhou, J. High Energy Phys. 07 (2021) 062.
[81] S.-Y. Hou, P. M. Saffin, Q.-X. Xie, and S.-Y. Zhou, J. High Energy Phys. 07 (2022) 060.
[82] M. S. Volkov and E. Wohnert, Phys. Rev. D **67**, 105006 (2003).
[83] B. Kleihaus, J. Kunz, and M. List, Phys. Rev. D **72**, 064002 (2005).
[84] E. Radu and M. S. Volkov, Phys. Rep. **468**, 101 (2008).
[85] Y. Brihaye and B. Hartmann, Phys. Rev. D **79**, 064013 (2009).
[86] L. Campanelli and M. Ruggieri, Phys. Rev. D **80**, 036006 (2009).
[87] H. Arodz, J. Karkowski, and Z. Swierczynski, Phys. Rev. D **80**, 067702 (2009).
[88] Y. Brihaye, T. Caebergs, and T. Delsate, arXiv:0907.0913.
[89] C. Adam, P. Klimas, J. Sanchez-Guillen, and A. Wereszczynski, Phys. Rev. D **80**, 105013 (2009).
[90] E. Radu and B. Subagyo, Phys. Lett. B **717**, 450 (2012).
[91] F. Navarro-Lerida, E. Radu, and D. H. Tchrakian, Phys. Rev. D **95**, 085016 (2017).
[92] G. Tallarita, A. Peterson, S. Bolognesi, and P. Bedford, Eur. Phys. J. C **80**, 38 (2020).
[93] H.-Y. Zhang, M. A. Amin, E. J. Copeland, P. M. Saffin, and K. D. Lozanov, J. Cosmol. Astropart. Phys. 07 (2020) 055.
[94] M. Dine, L. Randall, and S. D. Thomas, Phys. Rev. Lett. **75**, 398 (1995).
[95] M. Dine, L. Randall, and S. D. Thomas, Nucl. Phys. **B458**, 291 (1996).
[96] D. Daverio, M. Hindmarsh, and N. Bevis, arXiv:1508.05610.
[97] R. L. Higdon, SIAM J. Numer. Anal. **31**, 64 (1994).
[98] R. L. Higdon, Math. Comput. **47**, 437 (1986).